ELSEVIER

Contents lists available at ScienceDirect

# Materials & Design

journal homepage: www.elsevier.com/locate/matdes



# Taming geometric frustration by leveraging structural elasticity

Janav P. Udani, Andres F. Arrieta\*

Purdue University, United States



#### HIGHLIGHTS

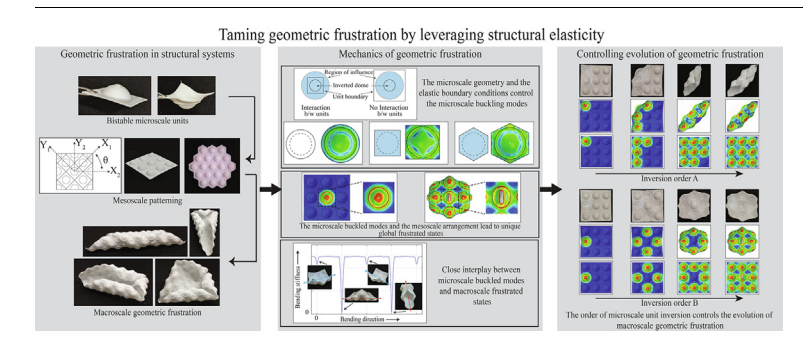
- Microstructure geometry "programs" the degree of macroscale geometric frustration.
- Macroscale frustration manifests as hierarchical multistable (coexisting global) states.
- Metasheet sustains multiple global frustrated states for the same loading conditions
- Spatiotemporal deformation path allows on-demand access to any global frustrated state.
- Taming geometric frustration enables machine-like mechanocomputing structural systems.

### ARTICLE INFO

Article history: Received 9 March 2022 Revised 27 May 2022 Accepted 30 May 2022 Available online 27 June 2022

Keywords: Geometric frustration Complex systems Programmable Structures Metamaterials Multistability

#### G R A P H I C A L A B S T R A C T



### ABSTRACT

Geometric frustration appears in a broad range of systems, generally emerging as disordered ground configurations, thereby impeding understanding of the phenomenon's underlying mechanics. We report on a continuum system featuring locally bistable units that allows for the controlled and self-sustained manifestation of macroscopic geometric frustration. The patterning of the units encodes a finite set of ordered ground configurations (spin-ice states) and a unique family of co-existing higher-order frustrated states (spin-liquid states), which are both activated upon unit inversion. We present a strategy for accessing any globally frustrated state on-demand by controlling the constitutive units' inversion sequence. This control strategy allows for observing the unfolding of geometric frustration as the microstructural features evolve due to the energy minimization of the constitutive units' interactions. More broadly, our model system offers a blueprint for "taming" macroscopic geometric frustration, enabling novel applications such as path-driven computation and solving optimization problems using structural systems.

© 2022 The Authors. Published by Elsevier Ltd. This is an open access article under the CC BY-NC-ND license

(http://creativecommons.org/licenses/by-nc-nd/4.0/).

# 1. Introduction

Geometric frustration arises when a lattice system cannot simultaneously minimize all of its local interaction energies due to constraints [1,2]. This leads to a high degree of degeneracy in the system, and the emergence of multiple disordered, high entropy ground configurations. This phenomenon is most com-

\* Corresponding author.

E-mail address: aarrieta@purdue.edu (A.F. Arrieta).

monly seen in ordinary water ice [1], wherein the hydrogen ions surrounding the central oxygen atom are arranged in a tetrahedral configuration to minimize the interaction energy. Interestingly, geometric frustration is also argued to have implications on the folding of proteins to form a well-defined structure with biological functionality [3]. The essence of this phenomenon is captured using a model of Ising spins with antiferromagnetic interactions arranged in a two-dimensional triangular lattice [4,5]. The three interaction energies cannot all be simultaneously minimized, resulting in two antiparallel spins, while the third is frustrated (Fig. 1a). This simple model is extrapolated to describe several

physical systems exhibiting frustration, including artificial spin-ice systems [6–12], colloid systems [2,13], periodically arranged magnetic rotors [14], acoustic channel lattices [15] and elastic structural systems [16–18]. However, the majority of these systems show high entropy, disordered states, which impede deeper understanding of the mechanics of geometric frustration. Therefore, there is a growing interest in establishing physical systems featuring ordered frustrated configurations, as a route to unveiling the intricacies of important processes such as natural protein folding [3], self-assembly of fibers [19,20] and nanotubules for targeted drug delivery [21], and memory storage in microelectronic devices [21,22].

Mechanical systems exhibiting deformation-driven frustration present an intriguing avenue for understanding the emergence of order in otherwise disordered systems. Cellular structures featuring beam [18] and shell units [16,23,24] have been shown to naturally exhibit unique and ordered global patterns that emerge either as a result of local elastic constraints or non-near neighbor (NNN) interactions. The mechanics for the emergence of degenerate states in elastic systems were first investigated by Mansfield, in his seminal work employing a prototypical thin plate subjected to a through-thickness temperature gradient [25,26]. For low thermal field values, the deformed configuration exhibits constant spherical curvature (positive Gaussian curvature,  $\mathcal{K} > 0$ ), characterized by both membrane and bending stresses. This spherical deformation results from the absence of any preferential direction for bending in the ideal circular plate. However, upon reaching a threshold in the external field value, the membrane stresses are released. This results in the plate bifurcating into a developable cylindrical form ( $\mathcal{K} = 0$ ), curling up about any diametrical axis (for an ideal plate). This leads to infinitely many post-buckled degenerate states (Fig. 1b). Invariably, imperfections in practical realizations control the orientation of the bending axis. Hence, while the possibility of achieving bending in any direction is fascinating and desirable for shape morphing, uncontrolled degeneracy renders it as a prohibitively complicated control problem. Furthermore, this concept and other examples of magnetic, colloidal and elastic frustrated systems rely on continuously applied external forcing fields for frustration to emerge, thus limiting the utilization of geometric frustration in practical applications.

We report on a classical mechanics lattice system that features controlled macroscale geometric frustration that is primarily driven by the bistability of the microscale units. The system is composed of bistable dome-like units arranged in a continuum metasheet. Local inversion (local buckling) of the domes introduces pre-stress in the system. The interactions between the inverted units' deformation fields result in global geometric frustration in the lattice (Figs. 1c-d). We note that the dome inversion and the ensuing geometric frustration are elastic and reversible in nature. Consequently, the emergence of geometric frustration is independent of the material properties as long as the inversioninduced stresses are within the failure limits (see Appendix A, Materials and Methods). The macroscale frustration in our system uniquely manifests in the form of hierarchical multistability [24,27], which we define as the emergence of multiple global states for a given dome inversion pattern. Hierarchical multistability departs from the characteristic one-to-one correspondence between the microscale and the macroscale states commonly found in mechanical metamaterials (Figs. 1e-f, see Appendix B for length scale definitions). The studied model lattice features four unique characteristics with regards to geometrically frustrated classical systems, namely: (i) local bistability allows for selfsupported pre-stress, thus eliminating the need for sustained external forcing fields to realize geometric frustration; (ii) the elastic constraints imposed by the units patterning naturally lead to the emergence of a finite set of ordered global ground configurations; (iii) in addition to the ordered ground states, the system displays selectively ordered-disordered configurations that closely resemble the spin-liquid states observed in condensed matter frustrated systems; and (iv) all the global hierarchical stable states can be achieved on-demand by controlling the interactions between the units through the history of dome inversions (i.e., the spatiotemporal deformation path). The designs, analyses, and results presented in this manuscript serve as general blueprints for studying geometric frustration at an accessible length scale, as well as enabling unique applications in mechanical computation, soft robotics [24] and morphing structures [28].

#### 2. Mechanics of deformation-driven geometric frustration

The inversion of local units results in the global out-of-plane bending of the metasheet, thus allowing for reversible 2D to 3D shape and property transformation (Figs. 1, 2). Similar to Mansfield's thin plates, the degeneracy in our system arises due to a non-unique cylindrical bending axis once a sufficient number of domes with interacting deformation fields are inverted. Contrary to the heated flat plates' case, the resistance to out-of-plane deformation is not uniform throughout the dome sheet. Instead, the resistance to bending is affected by the metasheet's topology, which is dictated by the patterning of the units. This purely geometric feature leads to a finite set of preferential global bending directions that limit the degree of degeneracy, thereby allowing for the controlled manifestation of geometrically frustrated macroscopic states. To better understand this characteristic, we adopt a homogenization scheme following Ref. [27], designed to model the emergence of global modes due to the variation in bending stiffness from dome inversions in the metasheet. We employ a simple square pattern for the analysis and the schematic in Fig. 2a outlines the relevant co-ordinate frames. The square patterned units are aligned with the  $X_1Y_1Z_1$  co-ordinate set; the frame is fixed with respect to the units but is free to rotate by the angle  $\theta$ with respect to a globally fixed frame  $X_2Y_2Z_2$ , such that  $X_1 = X_2 \cos(\theta) + Y_2 \sin(\theta)$  and  $Y_1 = -X_2 \sin(\theta) + Y_2 \cos(\theta)$ . Inverting the domes results in the metasheet adopting a curled configuration with an undulating profile that is modeled by a smooth function  $z = f_1(X_1, Y_1) = f_2(X_2, Y_2, \theta)$ , capturing the middle points' heights from the  $X_2Y_2$ -plane and assumed constant thickness t. Without loss of generality, we assume that cylindrical bending of the metasheet always occurs about the  $X_2$ -axis; this assumption does not impose any limiting constraints as the orientation of the domes  $\theta$  is set to be free with respect to the  $X_2$ -axis. Consequently, the bending stiffness can be expressed as,

$$B(Y_2) = E \int z^2 t dX_2, \tag{1}$$

where E is the elastic Young's modulus of the material. Next,  $\kappa(Y_2)$  is defined as the singly varying curvature of the middle plane, and thus, the angle subtended by the bent metasheet is,

$$\phi = \int \kappa(Y_2) dY_2 = \int \frac{M}{B(Y_2)} dY_2 \propto \int \frac{dY_2}{\int z^2 dX_2} = \frac{1}{\epsilon}, \eqno(2)$$

where M is any general bending moment leading to bending about the  $X_2$ -axis,  $\epsilon$  is a relative measure of the bending stiffness and linearity is assumed. With this setup, for any given z profile, the directions of least bending stiffness are identified by analyzing the variation in  $\epsilon$  as a function of the dome orientation  $\theta$ . We assume an idealized biharmonic profile  $z = \cos(nX_1)\cos(nY_1) = \cos(nX_2\cos(\theta) + Y_2\sin(\theta))\cos(n-X_2\sin(\theta) + Y_2\cos(\theta))$ , with  $X_2, Y_2 \in [-\pi, \pi]$  and, n defining the dome packing density, that qualitatively captures the undulating profile for an inverted square metasheet (Fig. 2b). The results indicate two well-defined minima

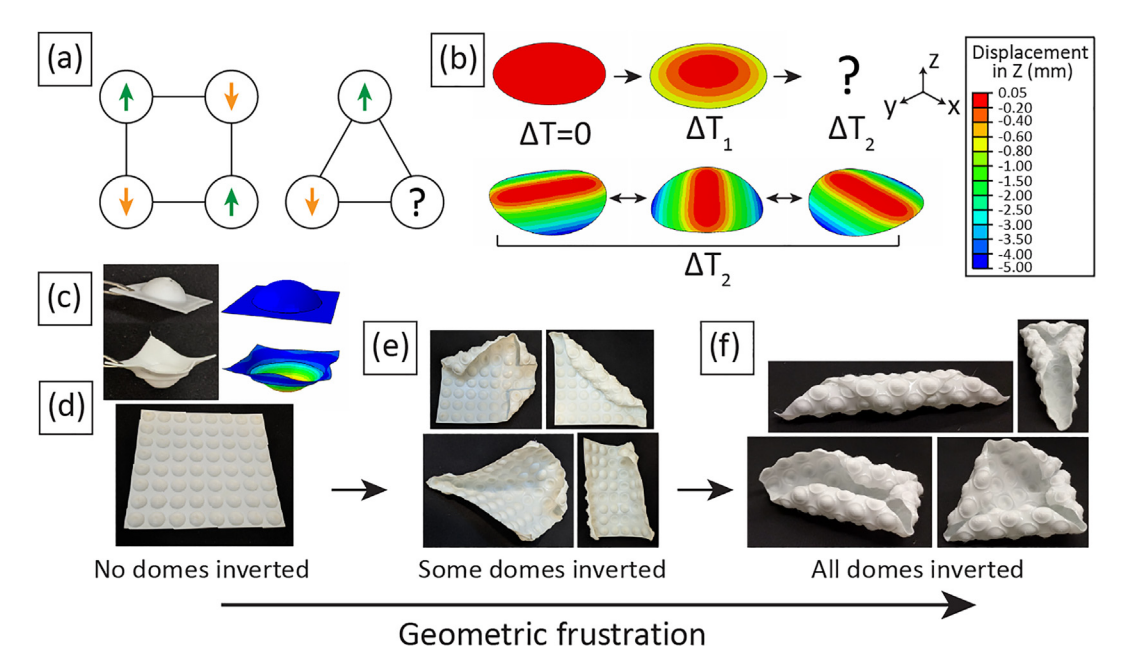
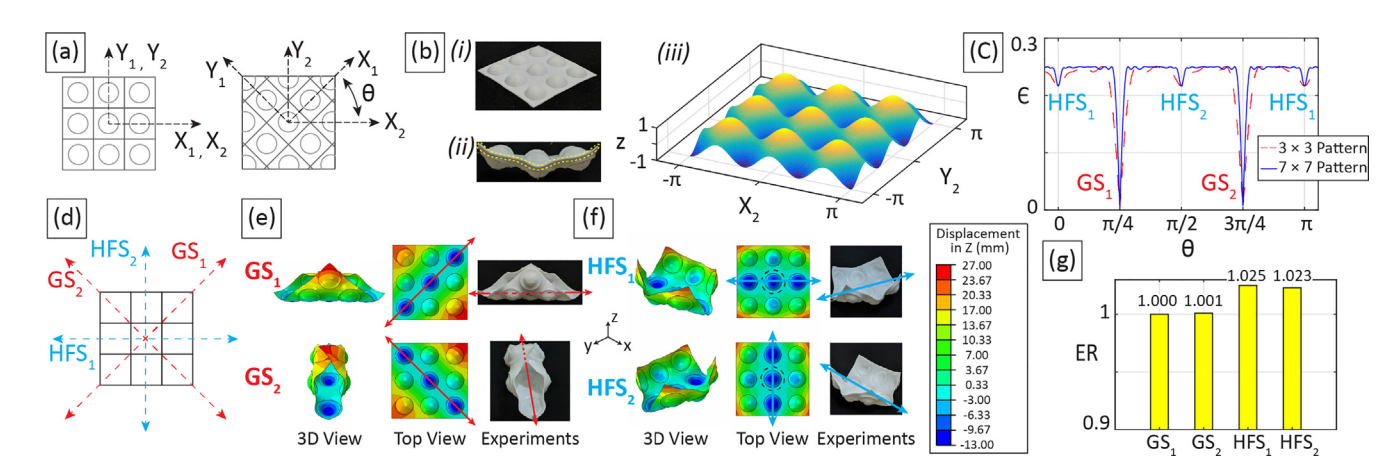


Fig. 1. (a) Schematic illustrating the Ising model. Antiferromagnetic interaction spins are satisfied on a square but cannot be satisfied in a triangular arrangement. (b) Structural degeneracy in heated thin plates. When the temperature gradient crosses a threshold value, the plate bifurcates from a spherical to a cylindrical bending configuration with a degenerate bending axis. (c) A dome unit in the base and inverted states (see SI video 1). (d) Square patterned dome metasheet (e) - (f) Manifestation of geometric frustration as an increasing number of domes are inverted.

in the  $\epsilon(\theta)$  plot, thereby suggesting the existence of two unique bending directions when a sufficient number of interacting domes are inverted. Interestingly, both the minimum bending stiffness orientations are aligned with the diagonals, i.e., with the two least packing directions of the square patterned units (Fig. 2d). This is confirmed by the FE and experimental results (Fig. 2e) (see Appendix A, Materials and Methods for details). This indicates the emergence of second neighbor interactions (long range interactions) in the frustrated stable states that develop as an increasing number of domes are inverted in the metasheet. The observed cylindrical configurations bear close resemblance to the ground state configurations seen in other examples of geometrically frustrated systems

as: (i) they have bending axes aligned with the programmed preferential directions; (ii) they exhibit identical strain energy levels (Fig. 2g); and (iii) they are reached when the maximum self-sustaining pre-stress field is introduced. The latter feature implies that inversion of all domes in the metasheet is analogous to freezing down to 0K in naturally frustrated systems. However, in contrast to the random and highly degenerate ground states seen in other systems, the dome metasheets sustain a finite *m*-dimensional manifold of ground configurations, *m* being the number of least packing directions that are programmed purely by virtue of the unit patterning in the metasheets. Finally, we note the emergence of second neighbor interactions in the ordered ground states in our system is



**Fig. 2.** (a) Schematic defining the co-ordinate frames employed in the homogenization model. (b) (i) Base state of the  $3 \times 3$  metasheet. (ii) Undulating profile when the domes are inverted (iii) Biharmonic function modeling the undulating profile in the inverted metasheet. (c)-(d)  $\epsilon(\theta)$  plot and schematic of the metasheet illustrating the minima in the bending stiffness orientations corresponding to the ground states (GS<sub>1</sub>, GS<sub>2</sub>) and higher-order frustrated states (HFS<sub>1</sub>, HFS<sub>2</sub>). (e)-(f) FE and experimental results illustrating the ground states and the higher-order frustrated states. The top view columns illustrate the deformation field corresponding to the respective state, over-plotted on the base state of the metasheet. The arrows indicate the bending axes for the respective states. (g) Strain energy levels associated with the four hierarchical stable states. The values are normalized as the Energy Ratio (ER) with respect to the strain energy associated with GS<sub>1</sub>.

not surprising as the mechanism of long range interactions leading to ordered global states has also been found in other classes of geometrically frustrated systems [12,18,29].

#### 3. Higher-order frustrated states

Besides the two global minima in the  $\epsilon(\theta)$  plot, there are two additional local minima oriented orthogonally to the unitpatterning directions of the metasheet. To investigate this feature we perturb the ground states in both FE and experiments by applying external mechanical forces and find that the local minima indeed correspond to additional physically stable global states for the same dome inversion pattern, i.e., all domes inverted (Fig. 2f; see SI video 2). Noticeably, these states exist at a higher strain energy level than the ground configurations (Fig. 2g). Consequently, these are associated with a shallower potential well in the global energy landscape, and the metasheet is easily perturbed out from these stable configurations. This observation is supported by the fact that the higher energy states feature a shorter bending axis compared to the ground states. Since the bending axis is equal to the side length in the former and equal to the diagonal length in the latter, the metasheet has a higher propensity to assume the more stable ground configurations. Based on the symmetry in the shapes and as observed in the  $\epsilon(\theta)$  modeling results, these higher energy states are uniquely characterized by the metasheet being "trapped" in a configuration between the two ground states. The metasheet has equal propensity to go to either of the ground states and in the process, assumes a higher energy frustrated configuration between two (already) frustrated ground states. We term these higher energy states as higher-order frustrated states. In a physical sense, these are characterized by the inability of the metasheet to release all of the membrane strain energy, thereby assuming a local minimum displaying stronger stretchingbending interactions. These are energetically unfavorable compared to their ground state counterparts, where the strain energy is primarily bending dominated. Finally, we note that the emergence of hierarchical multistable states is conditional on the inverted units' ability to introduce preferential global bending directions in the metasheet. We find that this feature stems from the interaction of the axisymmetric deformation field introduced by dome inversion with the boundary constraints imposed by the non-axisymmetrically packed units, and hence, is directly dependent on the packing density of the domes. We predict the associated design limits necessary for the manifestation of geometric frustration in our metasheet using an analytical approach modeling the topology of an inverted unit, as detailed in Appendix C.

# 4. Post-Buckling Trends: Breaking Unit Cell Deformation Symmetry

An interesting consequence of the multiple global frustrated states is the emergence of local higher-order buckling modes on the individual domes [30,31]. This feature is distinctly seen on the center dome in the higher-order frustrated states (black dashed circle in Fig. 2f), whereby the center dome departs from the locally axisymmetric (mirror-buckled) configuration to assume an elliptical shape with major axis aligned with the side of the square (see Appendix D). These local post-buckled shapes are again characterized by strong stretching-bending interactions, in contrast to the mirror-buckled state where the deformation is primarily bending dominated [32]. The emergence of local post-buckled shapes in our system is primarily dictated by two parameters, namely: (i) the individual unit design, a microscale property; and (ii) the global configuration that the system assumes following unit cell inversion, which is a macroscale property. Investigating the microscale design, we find that the flat's region geometry surrounding the dome plays a crucial role in the manifestation of local postbuckled shapes. The units' boundary shape largely dictates the elastic interactions with the neighboring inverted units (or in general any boundary conditions). When the interactions are strong, they impose a higher-order polygonal post-buckled shape on the central dome, moving away from the preferred axisymmetric

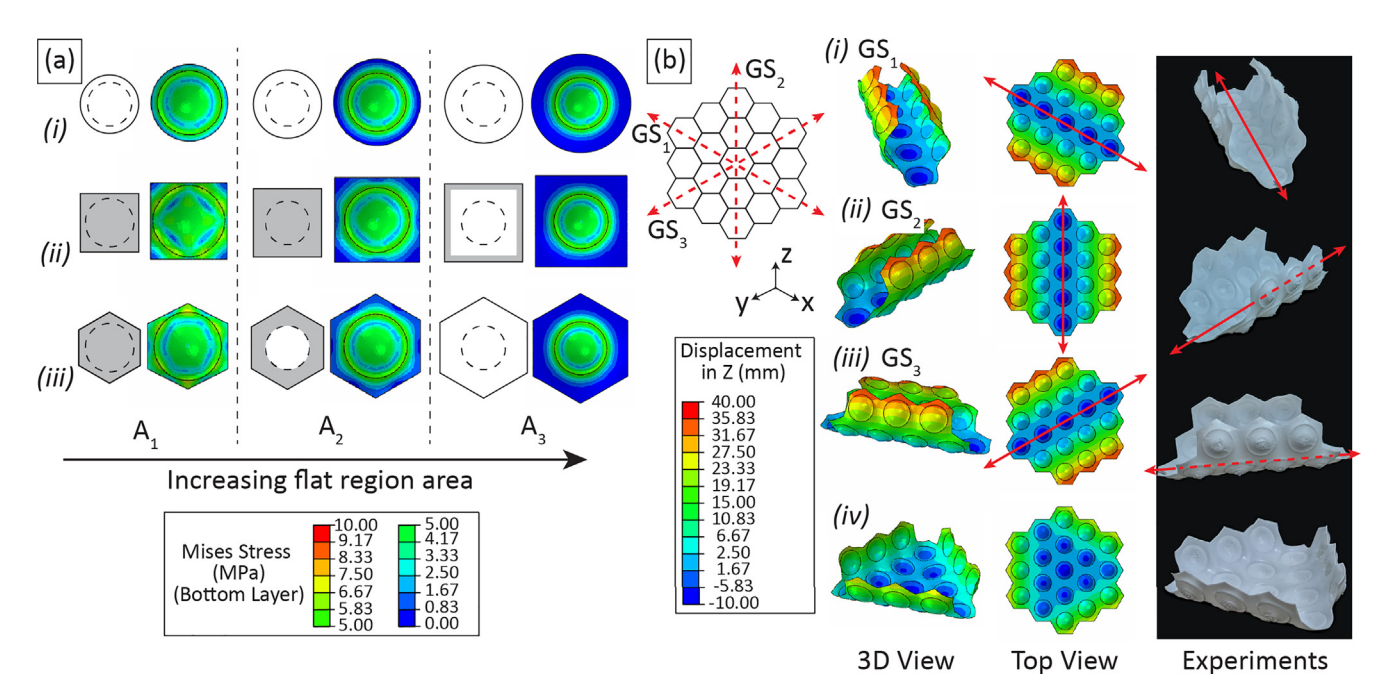


**Fig. 3.** (a) Higher-order post-buckling shapes for units featuring a (i) circular (ii) square and (iii) hexagonal boundary shape. The grey shaded area on the schematics indicates the region featuring a non-axisymmetric deformation state. The central dome reverts back to its preferred mirror-buckled state as the flat planform area increases or the number of symmetry axes in the boundary shape are increased. (b) The three bending axes and (i)-(iii) the associated ground states for a hexagonal metasheet. (iv) The higher-order frustrated state for the hexagonal metasheet displays a non-developable positive Gaussian curvature surface when all domes are inverted (see SI video 3). The top view column illustrates the deformation field corresponding to the respective state, over-plotted on the base state of the metasheet.

inverted shape. This characteristic is visualized in a simple experiment involving units with different geometries but equal flat region area (Fig. 3a). We pin the boundary edges to simulate the limiting case of the elastic constraints that are imposed on any individual unit in the metasheet when sufficient domes are inverted. The results indicate that for non-axisymmetric boundaries and a small flat region area, the edge constraints impose a non-axisymmetric post-buckled shape on the central dome in the inverted configuration. The break in axisymmetry originates from the boundary shape and is found to localize away from the dome center as the flat region area increases. Furthermore, the central dome regains an axisymmetric shape for smaller area values if the boundary shape features a higher number of symmetry axes (e.g., for a hexagon as compared to a square, Figs. 3a.(ii)-(iii)). In the limiting case of a circular planform, axisymmetry is never lost. This emergence of microscale higher-order buckling modes based on the unit geometry can be subsequently leveraged for programming the desired number of hierarchically multistable ground states at the macroscale. As illustrated in Fig. 2, a regular square pattern of the units features two preferential global bending directions. Similarly, a regular hexagonal pattern features three least packing directions due to the unit's symmetry, thus showing three degenerate global ground states after a sufficient number of units are inverted (Fig. 3b). Consequently, the microscale geometry can be tuned to program the desired number of macroscale ground states. However, triangles, rectangles and hexagons are the only polygonal geometries that can be arranged in a regular, completely packed 2D pattern. All other tessellations form irregular patterns and introduce broken symmetries, but in the process enable the ability to program non-uniform directions of least packing resulting in unique, irregular global shapes.

Along with the shape of the unit boundary, the metasheet's global deformed state also determines the post-buckling behavior of the individual domes. In general, the global ground states are characterized mainly by "concerted local buckling" of the microscale units. This is illustrated in Figs. 4a-b for square patterned metasheets. In these cases, the units assume elliptical post-buckled shapes with major axes diagonally aligned. Interestingly, this alignment direction coincides with the bending axis associated with each global ground state. Thus, there is an underlying order O<sup>GS</sup> for the (local) post-buckling behavior that propagates across all the units in the global ground states. A square patterned metasheet exhibits two ground state ordering trends,  $O^{CS} \in [O_1^{CS}, O_2^{CS}]$ , corresponding to the order associated with each preferential direction as programmed by the unit arrangement. The units' tendency to naturally and collectively orient towards their NNN in the postbuckled configuration again confirms the role of long-range interactions in the emergence of ordered global states, as previously discussed in the homogenization model results (Fig. 2). In contrast, analyzing the ordering trends in the units' post-buckling behavior for the higher-order frustrated states,  $O^{HFS}$ , no such long-range order similar to  $O^{GS}$  is evident. Instead, we find spatially distributed clusters of local order throughout the metasheet (Figs. 4c-d). This is mathematically expressed as  $O^{\textit{HFS}} \in \left[O_1^{\textit{HFS}}, O_2^{\textit{HFS}}, \ldots\right]$  , where,  $O_n^{HFS} = O_1^{LC}\Big|_{A_1} + O_2^{LC}\Big|_{A_2} + \ldots$  Here, each  $O_m^{LC}$  corresponds to a different order cluster. The ordering trend of the resulting  $n^{th}$  higherorder frustrated state  $O_n^{HFS}$  is determined by combining the covered areas  $A_m$  of each individual cluster  $O_m^{LC}$ . While the set of local order clusters can in principle be very large, we note that the microstruc-

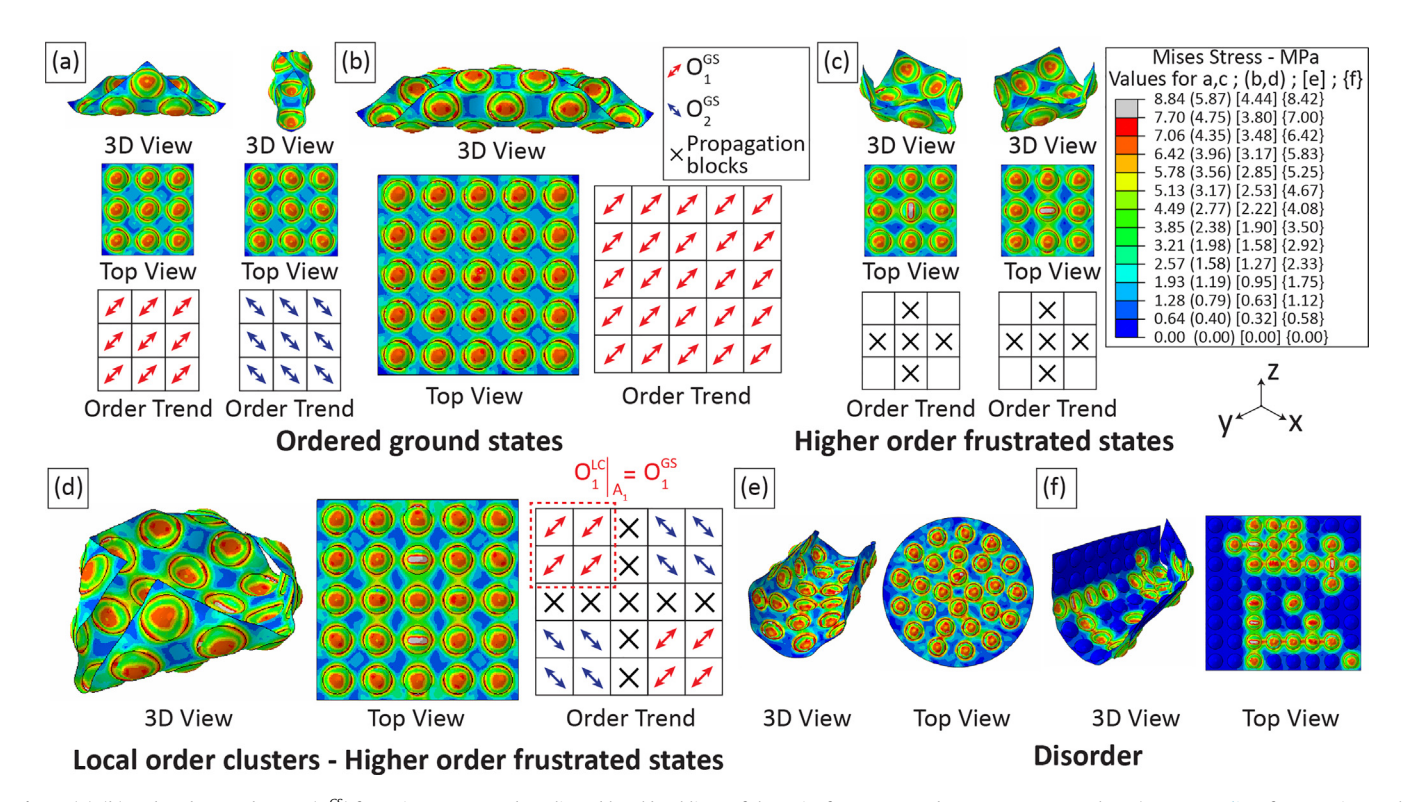


**Fig. 4.** (a)-(b) Ordered ground states ( $O^{CS}$ ) featuring "concerted or aligned local buckling" of the units for a 3 × 3 and 5 × 5 square metasheet (see Appendix E for experimental images of the 5 × 5 metasheet). (c)-(d) Local order clusters ( $O_m^{LC}$  example highlighted by the dashed red square in (d)) and non-developable deformation blocks preventing order propagation in the higher-order frustrated states  $O_m^{HE}$  for the respective metasheets. (e) Disorder within the microstructure achieved by random dome patterning and (f) when an insufficient number of interacting domes are inverted in the metasheets. The top view figures illustrate the deformation field corresponding to the respective state, over-plotted on the base state of the metasheet.

tural post-buckling shapes are still constrained by the unit design and the pattern-driven finite number of preferential bending directions encoded into the metasheet. Further inspection of the results in Figs. 4c-d reveals that order trends resembling both  $O_2^{GS}$  and  $O_2^{GS}$ are evident, albeit at different spatial locations for distinct groups of units. Neither of the ground state ordering trends has enough authority to force the metasheet into its respective global configuration. This results in deformation along diagonally opposite corners in a manner resembling both the ground states. However, the units in the center of the metasheet are trapped with equal propensity to adopt either state. As a result, the metasheet's central region assumes a locally non-developable deformation state impeding order propagation throughout. This non-developable region characterizes all the higher-order frustrated configurations and is essential for their emergence. In general, as the number of units is increased, there is an increased propensity for the emergence of different local order clusters, and the ensuing higherorder frustrated states (Fig. 1f). A similar trend is also expected for metasheets featuring a rectangular  $m \times n$  arrangement of domes. While the underlying states are still governed by the non-nearest neighbor interactions, the global deformed state of the metasheet plays a non-trivial role in determining the postbuckling behavior of the microscale units. Consequently, the unequal lengths of the edges of the rectangular planform could potentially have the propensity to induce distinct higher-order frustrated states, than what are seen on the square counterparts.

Interestingly, the appearance of local order clusters in the higher-order frustrated states of our dome metasheets is qualitatively reminiscent of the spin-liquid regime found in temperature-driven magnetic frustrated systems [1,33]. When such magnetic systems are cooled below the Curie–Weiss temperature, the spins form into local clusters with strong interactions that obey the ground state constraints, albeit, there is no long range propagation of the associated order within the system. This absence of long range order propagation is the precise characteristic that we find in the higher-order frustrated states in our dome metasheets. Further, we uniquely find that stable configurations

qualitatively resembling both the spin-ice regime (ground-state configurations) and the spin-liquid regime (higher-order frustrated states) can co-exist for the same input conditions on our system. For example, when all the domes are inverted, we find both the developable ground states (ordered spin-ice states) and the higher-order frustrated states (spin-liquid states) as illustrated in Figs. 4a-d. With this characteristic, our system joins an exclusive group of exotic systems exhibiting the co-existence of these two distinct stability regimes [34–37]. The appearance of both families of states in our system is a purely elastic consequence (compatible with different material chemistries, see Appendix E) determined by the programmed preferential bending directions and how much of the stored membrane energy – added by virtue of dome inversion at the microscale - is released at the macroscale. In essence, this co-existence of two qualitatively distinct stability regimes for the same input conditions is a result of the intriguing interactions at play between structural elasticity and geometric frustration in our continuum lattice system.

Finally, local disorder can also be programmed into the microstructure by randomly patterning the domes in the metasheet (Fig. 4e). In such cases, inverting all domes results in a complex energy landscape featuring global shapes with no clearly defined preferential bending directions. These degenerate global shapes feature a microstructure consisting of inverted domes that assume random and strongly disordered post-buckled shapes. In these designs, the interactions between structural elasticity and geometric frustration are not meaningfully leveraged, yielding macroscale shapes that while unique, are neither robust nor easily controllable. Additionally, disordered configurations in the microstructure also emerge when an insufficient number of interacting domes are inverted, resulting in limited authority to impose the programmed shape on the macrostructure (Fig. 4f). However, in general, we find that by leveraging the interactions between pattern-driven elastic constraints and deformation-driven geometric frustration, the prevalent behavior is ordered configurations, whereas disordered configurations need to be intentionally programmed into the system.

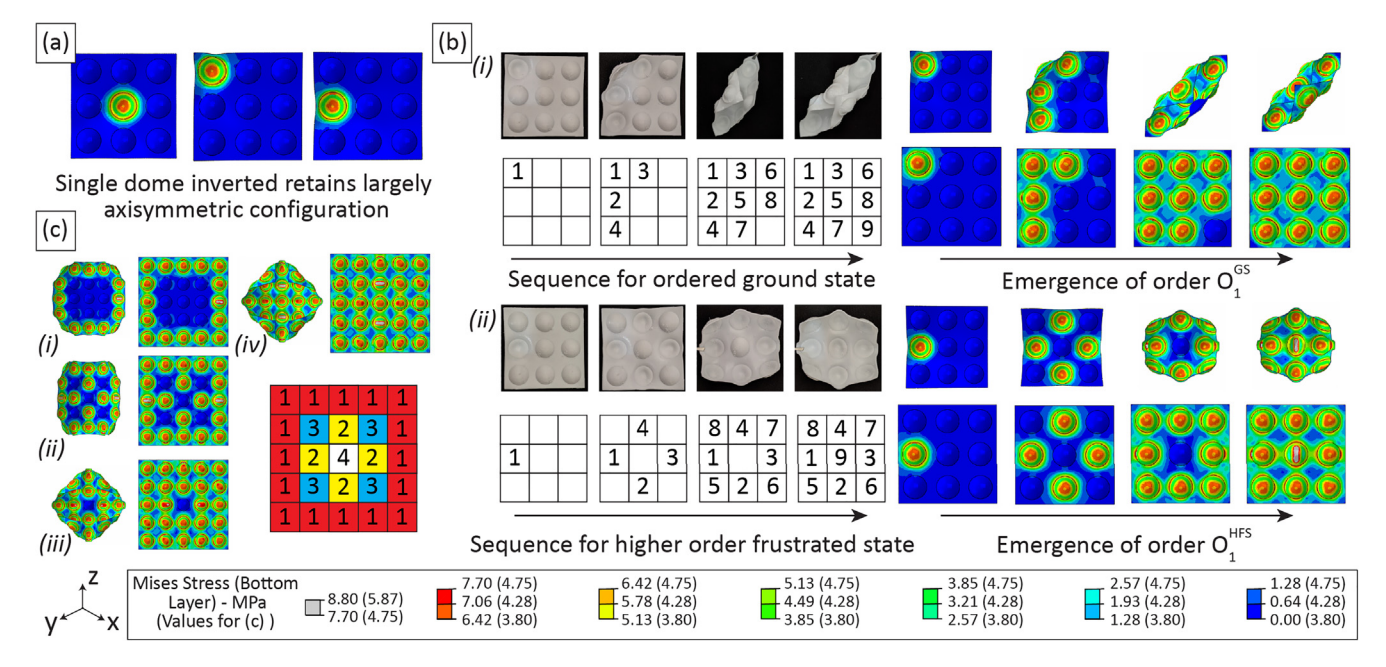


**Fig. 5.** (a) Single inverted dome retains a largely axisymmetric configuration. (b) Different dome inversion sequences leading to the desired global frustrated states for the  $3 \times 3$  square metasheet. (i) Diagonal inversion sequence leading to the ordered ground state. (ii) Diamond-like symmetric inversion sequence leading to the higher-order frustrated state. (c) Dome inversion sequence (i) - (iv) leading to a higher-order frustrated state for the  $5 \times 5$  square metasheet. All the FE simulation results are displayed in the top view. For (b) and (c), the plot pairs for each state correspond to the top view of the deformed configuration and the top view of the deformed field over-plotted on the base configuration.

# 5. Accessing the desired frustrated states on-demand: A control strategy

As noted before, the post-buckled shape and orientation of the units characterizes the global frustrated states. These characteristics can be further leveraged to achieve on-demand access to any desired global frustrated state. A dome unit is stress-free in its base state and assumes a stressed configuration only upon inversion. When a single unit is inverted, it assumes the axisymmetric mirror-buckled shape (Fig. 5a). However, as an increasing number of interacting units are inverted, the domes progressively transition into one of their polygonal post-buckled shapes depending on the sequence in which the interactions and elastic constraints are imposed. This feature can be leveraged to achieve any desired order, i.e.,  $O_n^{GS}$  or  $O_n^{HFS}$ , within the microstructure. Collectively, these interactions force the macrostructure to assume the specific global frustrated state corresponding to the respective microscale ordering scheme. Thus, distinct global frustrated configurations corresponding to the same inversion pattern can be readily accessed simply by controlling the dome inversion sequence. This concept is illustrated on a prototypical  $3 \times 3$  square patterned metasheet. When the dome inversion sequence is initiated in a diagonal sense, i.e., inverting a series of second neighbor domes from one corner to the other, the metasheet assumes the corresponding ground state configuration (Fig. 5b.(i), see SI video 4). In contrast, if the dome inversion sequence is initiated symmetrically about the center dome, implying we first invert the four middle domes in a diamond fashion and subsequently invert the four corner domes, we find that the diagonally-aligned bending axis necessary for reaching either of the ground states is not activated as the central dome is still in its base, stress-free state (Fig. 5b.(ii)). This inversion sequence imposes a configuration symmetrically aligned with either of the ground states, thus leading to the higher-order frustrated state when the center dome is finally inverted (see SI video 5). Similar inversion sequences can also be realized for larger metasheets by selectively imposing the desired microscale interactions between units; an example inversion sequence leading to a higherorder frustrated state for a  $5 \times 5$  square metasheet is shown in Fig. 5c (also see SI video 6). Noticeably, this strategy reveals that the mapping of the number of inversion sequences to the total number of frustrated states is not unique; the number of sequences is N!. N being the number of domes, and is presumably larger than the set of global frustrated states. While there may be multiple paths leading to a given global state, we note that no single path can guide the system into two frustrated states. This observation renders the inversion sequencing strategy as both robust and reliable in controlling the manifestation of geometric frustration in our system.

## 6. Outlook and Conclusions

In this work, we present a classical mechanics system displaying geometric frustration that can be controlled by the inversion (i.e., loading) sequence of its bistable units. We unveiled the mechanisms through which geometric frustration emerges using analytical tools and FE analysis. We establish geometric frustration as the phenomenon responsible for the hierarchical multistable behavior of the metasheet model system. We leverage the elastic constraints imposed by the domes' local bistability as a mechanism for selectively reaching the desired microscale interactions needed to realize distinct global frustrated states. This is a powerful concept that enables our system to serve as a testbed for accessibly studying the mechanisms governing geometric frustration, as well as for opening avenues for novel applications like path-driven computation

paradigms in structural systems [24]. More generally, the ability to "tame" geometric frustration enables the design of machinelike structural systems that serve as physical embodiments of complex optimization problems. The co-existing hierarchically multistable states discretize the system's configuration space into distinct, albeit finite minimum energy points. In this regard, the ground (ordered spin-ice) and higher-order frustrated (spinliquid) states correspond to global and local minima, respectively. The ability to separate and achieve any global frustrated state ondemand as controlled by distinct sequences of discrete external events (i.e., the local dome inversions and their history) sets a physical paradigm for mechanical optimization and information processing. In this regard, the presented dome metasheets open an avenue for implementing discrete optimization paradigms, both exact algorithms like the branch and bound [38] and metaheuristics like simulated annealing [39], into mechanical metamaterials. The macroscale deformation enables in situ monitoring of the optimization process or unfolding of geometric frustration, whereby iterative dome inversions allow for reaching the global minimum or ground state if required. The ability to encode the desired number of ground states (global minima) further enriches the optimization and computation paradigm afforded by our metamaterial architecture and enables the physical mapping of Paretooptimality. These features are absent in the general class of frustrated systems that exhibit uncontrolled degeneracy, and consequently, inhibit the ability to achieve a desired frustrated state on demand. Contrary to unfrustrated systems with a single global energy minimum, hierarchical multistability enables the mapping of richer optimization paradigms with complex energy landscapes.

Notably, our system naturally exhibits non-volatile memory at the microscale. The local bistable states of the units can be ascribed to bit values "0" and "1" [40,41]. This feature, complimented with the intrinsic deformation-driven optimization paradigm in our metasheets, provides a unique information processing capability on mechanical metamaterials. These characteristics paired together enable our geometrically frustrated metasheets to display a finite-state machine type behavior that solves optimization problems based on external inputs, internal unit states (bit values), and also stores long-term event history memory. We envision our system as a blueprint for achieving controlled interactions between structural elasticity and geometric frustration, leading to novel metamaterials with path-driven morphological computation capable of parsing spatially complex mechanical information for soft robotics [42-45], haptic devices [46,47], wearables, and adaptive aerospace systems [48,49].

# **Data Availability**

The raw/processed data required to reproduce these findings cannot be shared at this time due to technical or time limitations.

#### **Declaration of Competing Interest**

The authors declare that they have no known competing financial interests or personal relationships that could have appeared to influence the work reported in this paper.

### Acknowledgments

The authors acknowledge the support of the NSF-CAREER award No. 1944597 and the DSO DARPA-NAC award, contract No.  $\rm HR00112090010$ .

#### **Appendix A. Materials and Methods**

#### A.1. Experimental Specimen Design and Manufacturing

The experimental specimens are manufactured using Fused Deposition Modeling (FDM) 3D printing. The specimens are first modeled in SolidWorks 2016. The 3D files are then sliced using Ultimaker Cura 4.3.0 and printed on an Ultimaker 3+ using white thermoplastic polyurethane, supplied as Ultimaker TPU 95A (white). The specimens are printed flat on the print bed with material extruded from a single nozzle.

# A.2. Details on Finite Element (FE) Analyses

For the FE analysis, the specimens are modeled using Abaqus/ CAE 2018 and Python scripting. A linear-elastic material formulation for TPU is employed for the simulations with an elastic modulus of 51 MPa and Poisson's ratio 0.3. The effective elastic modulus for Ultimaker TPU 95A (white) is determined by conducting dogbone tests in-line with the ASTM D638 standard (Fig. A.1). Six dogbone samples are tested, each at two different loading rates. The results indicate that the different strain rates do not have any significant effect on the measured modulus of the TPU (Fig. A.1), and hence a linear-elastic material model is employed for the FE simulations. The simulation consists of multiple loading steps for dome inversion and each loading step is followed by two/three relaxation steps to allow the sheet to relax after each inversion event. Additionally, the metasheets are pinned at the center over the entire simulation to avoid any rigid body motion. The specimens are then meshed with a seed size of ≤ 2mm using a quaddominated mesh (shell elements). Diving into the loading details, individual domes are sequentially inverted in each loading step (Dome 1 in LoadStep-1, Dome2 in LoadStep-2, and so on) by an applied displacement (velocity)-load at the domes' center while constraining the internal and external edges of the specimen. The boundary conditions are released in the subsequent relaxation steps to allow the specimen to relax in the deformed global configuration following each dome inversion cycle, thus simulating a programmed sequence of dome inversion events on the metasheet. Numerical damping factor values of  $\leq 10^{-6}$  are defined for each step in the simulation. Finally, the simulations are solved with Abaqus/Standard (implicit formulation) on the Brown community cluster at Purdue University. A single node on the Brown cluster features 24 processor cores and 96 GB of RAM.

For the higher-order frustrated states in Fig. 2 in the main text, following dome inversion and subsequent relaxation, small loads are applied at specific control points on the metasheet. The location and orientation of these small displacement loads are chosen

to favor one of the co-existing hierarchical states. The sheet is again allowed to relax after load application and is allowed to settle in the desired stable hierarchical state.

For the  $3 \times 3$  and  $5 \times 5$  metasheets' ground state configurations (Figs. 2, 4, and 5 in the main text), the specimens exhibit self-contact when all the domes are inverted. To account for this, General Contact (Standard) interaction property is defined for the respective metasheets. The self-contact formulation models frictionless tangential behavior and the system default normal contact behavior, i.e., "hard" contact pressure-overclosure and default constraint enforcement method. Additionally, to render the  $5 \times 5$  metasheet simulations time efficient, the solver formulation is switched to Dynamic-Implicit, Quasi-Static for all of the loading steps and some of the relaxation steps. Accordingly, we use a density of  $1.22 \text{ g/cm}^3$  for the material formulation [50].

#### A.3. Details on Analytical Modeling

We use the symbolic manipulation software Wolfram Mathematica 9 for implementing both of the analytical formulations employed in this work, i.e., the homogenization model for finding the dominant global deformation modes and the Rayleigh–Ritz model for investigating the topology of the deformed axisymmetric units. The models are solved for in Mathematica and the data is subsequently exported for plotting and post-processing in MATLAB R2016b.

#### A.4. Dimensions of specimens employed in the manuscript figures

#### A.4.1. $3 \times 3$ square metasheets

The  $3 \times 3$  square metasheets illustrated in Figs. 2, 4, and 5 in the main text feature dome units with dome base radius, R=8 mm, dome height, h=5 mm, unit thickness t=0.7 mm, and unit side length, SS=22.4 mm. For the square metasheets, the unit side length is equal to the spacing between two nearest neighbor dome centers.

#### A.4.2. Unit cell buckling analysis

The specimens employed for the unit cell buckling analysis in Fig. 3 in the main text have dimensions, R=8 mm, h=5 mm and, t=0.5 mm. The three different planform area values for the flat regions are  $A_1\approx 122.93$  mm<sup>2</sup>,  $A_2\approx 282.93$  mm<sup>2</sup> and,  $A_3\approx 582.93$  mm<sup>2</sup>.

# A.4.3. Hexagonal metasheets

The hexagonal metasheets in Fig. 3 in the main text have dimensions R = 8 mm, h = 4 mm, t = 0.5 mm and spacing between two nearest neighbor dome centers, SS = 23.2 mm.

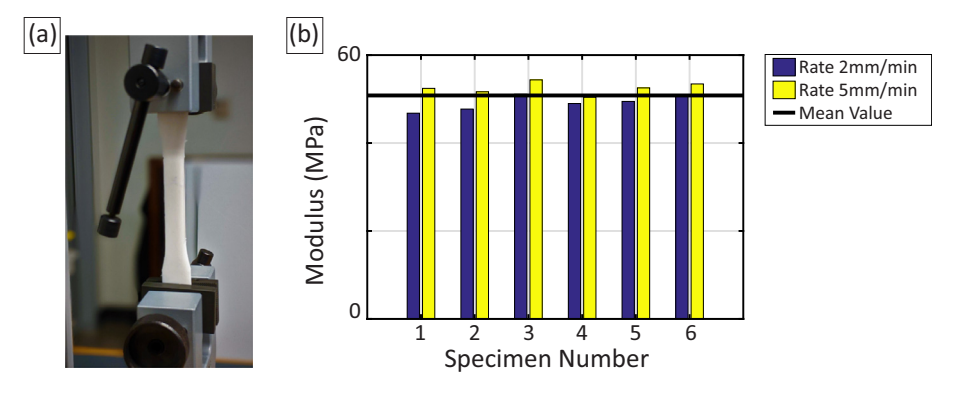


Fig. A.1. (a) Dogbone test for determining the modulus of white Ultimaker TPU 95A. (b) Post-processed results indicating the modulus for 6 different specimens, each tested under two different loading rates.

#### A.4.4. $5 \times 5$ square metasheets

The  $5 \times 5$  square metasheets in Figs. 4 and 5 in the main text have dimensions R = 8 mm, h = 4 mm, t = 0.5 mm, and SS = 22.4 mm.

#### A.4.5. Random pattern metasheet

The random pattern metasheet in Fig. 4 in the main text has dimensions, R = 8 mm, h = 4 mm and, t = 0.4 mm.

#### A.4.6. $8 \times 8$ square metasheet

The 8  $\times$  8 square metasheet in Fig. 4 in the main text has dimensions R=8 mm, h=5 mm, t=0.625 mm and SS=20.8 mm.

A.4.7. Specimens for studying hierarchical multistability boundaries The specimens in Figs. C.1 and C.3 have dimensions R = 8 mm, h = 5 mm, t = 0.625 mm and SS is varied.

# Appendix B. Length scale definitions in the analysis of dome patterned metasheets

The dome patterned metasheets analyzed in this study are characterized by a hierarchical structure spanning three different length scales (Fig. B.1). Characteristic features at each of the three length scale combine together to allow for the unique property-set and hierarchical multistable behavior at the global scale. Accordingly, the different length scales are defined as:

- Microscale The microscale comprises the individual units. The local dome dimensions and the dimensions of the flat region constitute the microscale design. Additionally, the inversion of the domes and the local post-buckling behavior of individual units are also microscale features.
- 2. **Mesoscale** The mesoscale consists of the patterning of the local dome units. For example, the square and hexagonal patterned metasheets featuring identical dome units are distinguished from each other at the mesoscale. Similarly, regular v/s irregular tessellations, ordered v/s random patterns are all mesoscale design parameters.
- 3. **Macroscale** The macroscale characterized the global behavior of the metasheet. The globally deformed configurations that the metasheet assumes as the domes are inverted constitute the macroscale. Accordingly, the hierarchical states are distinguished from each other at the macroscale.

# Appendix C. Analytical model for predicting the boundaries of hierarchical multistability

Geometric frustration in our metasystem and the ensuing hierarchical multistability characteristics only manifest when a sufficient degree of pre-stress is inputted into the system, as with the temperature-driven degenerate bending plates [25,26]. This invariably corresponds to the pre-stress introduced via dome inversion and its propensity to introduce preferential bending directions in the dome metasheets. If the domes are packed in a sparse manner, the metasheet in the all domes inverted state assumes a nondevelopable, bent configuration, qualitatively similar to that seen for low thermal field values in the bending plates (Fig. C.1a). As the packing density of the domes is increased beyond a certain threshold, the metasheet bifurcates into a developable form as the domes are inverted in the system. We identify the packing ratio, i.e., the ratio of the unit side length (S) to the radius of the dome (R),  $(PK = \frac{S}{R})$  as a critical parameter governing this bifurcation in the metasheets. This observation stems from the fact that inversion of a dome results in axisymmetric out-of-plane bending of the flat region surrounding the dome. This axisymmetric out-ofplane deformation field interacts with the non-axisymmetrically shaped boundary leading to the non-uniform bending resistance central to the manifestation of the preferential bending directions at the macroscale. However, if the packing factor is sufficiently large, such that the flat region of any given unit extends beyond the radius of influence of the inversion-induced field, the interplay between the non-axisymmetric boundary shape and the axisymmetric deformation field is lost (Fig. C.1b). This excess region offers largely uniform bending resistance in all directions and, consequently, the metasheet loses preferential bending directions and starts behaving like a flat sheet subjected to external loading.

We capture this bifurcation between hierarchical to non-hierarchical global behavior employing an analytical approach modeling the topology of an axisymmetric unit in the inverted state. Specifically, we model the topology as the microscale packing factor PK is varied, inspecting the change in the gradient  $(\lambda_r)$  at the flat region's boundary for each design. A zero-crossing in the  $\lambda_r(PK)$  plot marks the limit beyond which the flat region topology is unaffected by the inversion induced deformation field, thereby indicating the loss of hierarchical multistability.

We employ the Föppl-von Kármán equations (assuming axisymmetry) in the radial co-ordinates r and  $\theta$ ,

$$D\nabla^4 w - \frac{t}{r} \frac{\partial}{\partial r} \left[ \frac{\partial w}{\partial r} \frac{\partial \Phi}{\partial r} \right] = 0 \quad \& \quad \frac{\nabla^4 \Phi}{E} + \frac{1}{r} \frac{\partial w}{\partial r} \frac{\partial^2 w}{\partial^2 r} = 0, \tag{C1}$$

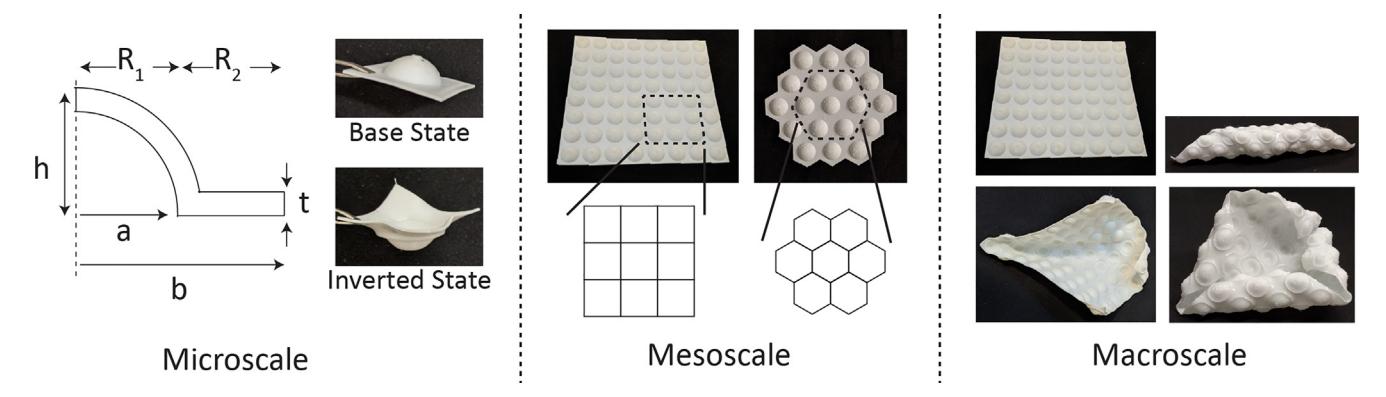


Fig. B.1. The different length scales involved in the design and analyses of the hierarchical metasheets.

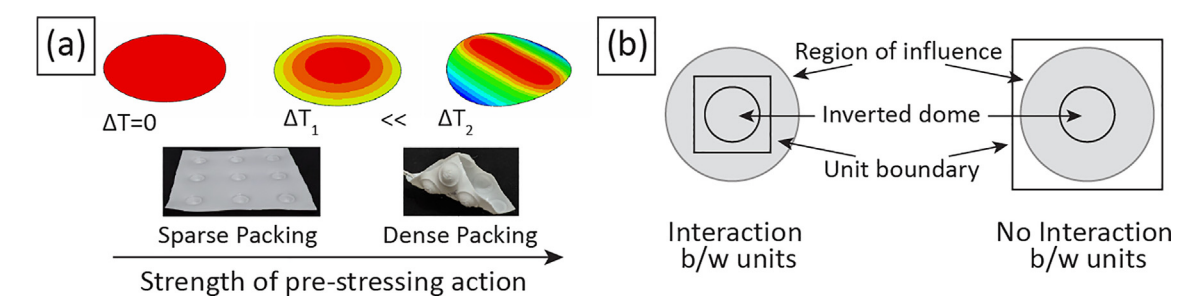
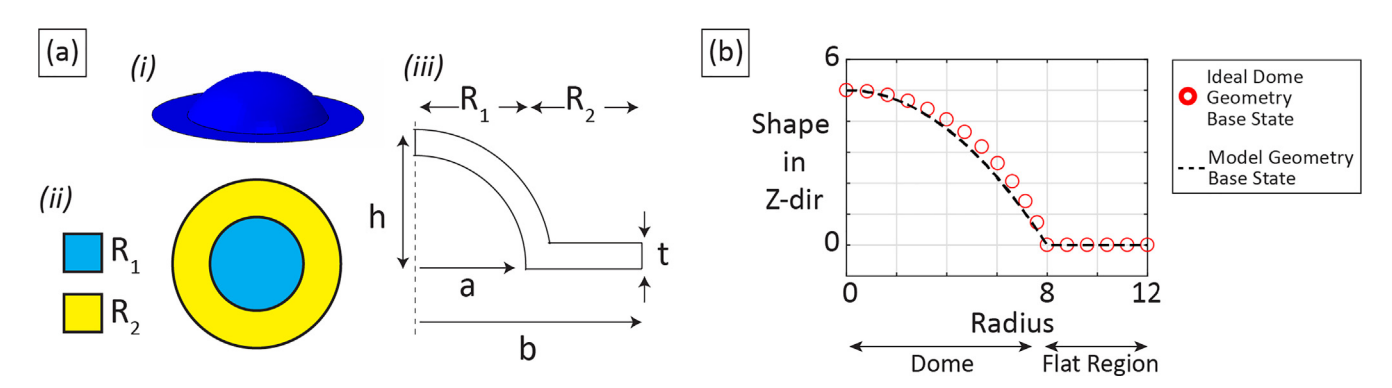
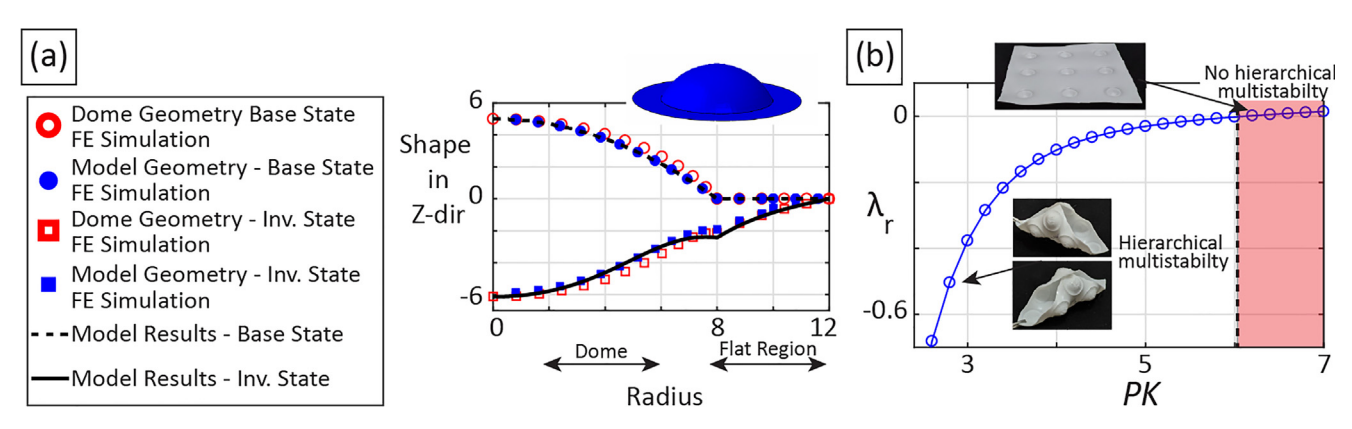


Fig. C.1. (a)-(b) Geometric frustration manifests only when the domes are sufficiently densely packed and the region of influence of the deformation field following dome inversion exceeds beyond the unit boundary.



**Fig. C.2.** (a) (i) The axisymmetric dome unit. (ii)-(iii) The different design parameters and the regions  $R_1$  and  $R_2$  involved in the analysis. (b) Topology of the axisymmetric unit employed in the analytical model as compared to the ideal dome geometry. The red markers correspond to the actual dome geometry. The black dashed line corresponds to the mathematical function approximating the dome geometry that is employed for the analytical model.



**Fig. C.3.** (a) Topology of the inverted axisymmetric unit as predicted by the analytical model and FE simulations. The red markers correspond to FE results for the actual dome geometry. The blue markers correspond to FE results for the mathematical function approximating the dome geometry that is employed for the analytical model (Eq. (2)). (b)  $\lambda_r(PK)$  plot illustrating the model predicted boundary separating hierarchical and non-hierarchical design regimes. The insets illustrate experimental examples of the respective designs.

where,  $D = \frac{Et^3}{12(1-v^2)}$  is the flexural rigidity, and  $\Phi$  and E are the Airy's stress function and elastic Young's modulus respectively. Following Ref. [51], we decouple Eqs. (C1) into their stretching and bending components and solve for the stable states by Rayleigh–Ritz minimization of the total potential energy.

The unit is divided into two distinct regions: (i) the central initially curved dome; and (ii) the surrounding flat region (Fig. C.2a). We start by assuming an initially curved shape for the unit as,

$$w_{R1}^0 = (1 - \rho^2) w_m^0 \quad \& \quad w_{R2}^0 = 0,$$
 (C2)

where,  $w_{R1}^0$  and  $w_{R2}^0$  are the initial displacements of the central dome and the flat region respectively,  $\rho = \frac{r}{a}$  is the dimensionless radial parameter, with a being the base diameter of the dome and  $w_m^0$  is the initial midpoint deflection of the dome. The geometry assumed in Eq. (C2) is an approximation of the ideal dome geometry. Nonetheless, the results are found to be in good agreement with the actual dome FE results (see Fig. C.2b and Fig. C.3). As discussed in the main text, the initial or the base state of the unit is stress-free. Next, we denote the displacement of the inverted, stressed configuration by  $w_{R1}$  and  $w_{R2}$  for the dome and the flat region respectively. Accordingly, the change in displacement is given by

 $\hat{w}_{R1} = w_{R1} - w_{R1}^0$  and  $\hat{w}_{R2} = w_{R2} - w_{R2}^0$  respectively. The gradient  $(\lambda_r)$ , radial and circumferential curvature  $(\kappa_r$  and  $\kappa_\theta)$  terms are derived from the displacement expressions for the respective states as,

$$\lambda_r = -\frac{\mathrm{d}w}{\mathrm{d}r}, \quad \kappa_r = -\frac{\mathrm{d}^2w}{\mathrm{d}r^2} \quad \& \quad \kappa_\theta = -\frac{1}{r}\frac{\mathrm{d}w}{\mathrm{d}r}, \tag{C3}$$

and the variations in the respective terms  $(\hat{\lambda}_r, \hat{\kappa}_r \text{ and } \hat{\kappa}_\theta)$  between the initial and the final states follow naturally. Correspondingly, the principal bending moments and the shear stress terms are defined as,

$$m_r = D(\kappa_r + \nu \kappa_\theta), \quad m_\theta = D(\kappa_\theta + \nu \kappa_r) \quad \& \quad q_r = \frac{\mathrm{d}m_r}{\mathrm{d}r} + \frac{m_r - m_\theta}{r},$$
 (C4)

where, v is the Poisson's ratio and linear elastic, isotropic material behavior is assumed. Again, since the base state is stress free, the change in the respective quantities in Eq. (C4) is equal to the final value of the quantities, i.e.,  $\hat{m}_r = m_r$ ,  $\hat{m}_\theta = m_\theta$ , and  $\hat{q}_r = q_r$ . Lastly, all of the quantities in Eqs. (C3) and (C4) are calculated for both of the dome and the flat regions, i.e., R1 and R2.

For the Rayleigh-Ritz formulation, we assume a polynomial series expansion for the change in the radial curvature for both of the

regions in the unit, i.e.,  $\hat{\kappa}_r = \sum\limits_{i=0}^n c_i r^i$ , and the other quantities are

then calculated in terms of the generalized co-ordinates,  $c_i$ . This results in two additional constants for each region in their respective displacement expressions originating due to the double integration operation for transforming between the two fields. These additional constants are satisfied by imposing the boundary conditions (BC) and continuity conditions in the out-of-plane problem. For this formulation, we assume that the unit is pinned at its outermost boundary. This assumption is an idealization of the more realistic spring-type BC that is levied by the surrounding elastic continuum on any given unit in the metasheet. However, we find that the results obtained by following a pinned outer edge BC allow for a conservative estimate of the limits on hierarchical multistability in our metasheets. A more precise bound can be obtained by augmenting the model in it's current form with springs assumed at the edges. The pinned BC for the out-of-plane problem can be mathematically expressed as,

$$w_{R2}|_{r=b} = 0 \quad \& \quad m_{r-R2}|_{r=b} = 0.$$
 (C5)

Additionally, for the full dome with no slits/cuts, we have two other conditions for the center point of the unit that are expressed as,

$$q_{r-R1}|_{r=0} = 0 \& \frac{\partial w_{R1}}{\partial r}|_{r=0} = 0.$$
 (C6)

These BCs for the out-of-plane problem (Eqs. (C5) and (C6)) are further augmented by considering the elastic continuity conditions for the displacement and the slope at the boundary connecting the dome to the surrounding flat region,

$$w_{R1}|_{r=a} = w_{R2}|_{r=a} \quad \& \quad \frac{\partial w_{R1}}{\partial r}|_{r=a} = \frac{\partial w_{R2}}{\partial r}|_{r=a}.$$
 (C7)

This set of six constraint equations in the out-of-plane problem is first employed to solve for the four constants resulting from the double integration operation to find the displacement fields from the assumed curvature expressions. The remaining constraint expressions are satisfied by reducing the number of degrees of freedom by the corresponding amount. For example, for the full dome shell, considering only even terms in the assumed curvature expression automatically satisfies the BC for the shear force (Eq. (C6)), thus simplifying the model and improving the computational efficiency. Additionally, we find that considering four terms in the assumed curvature fields for each of the regions allows for sufficient accuracy

in modeling the topology of the inverted unit. Accordingly, the assumed expressions for the change in the radial curvature are given as,

$$(\hat{\kappa}_r)_{R1} = \sum_{i=0}^4 (c_i)_{R1} r_{R1}^{2i} \quad \& \quad (\hat{\kappa}_r)_{R2} = \sum_{i=0}^4 (c_i)_{R2} r_{R2}^i.$$
 (C8)

Next, moving on to the in-plane problem, we employ the Airy's stress function,  $\Phi$ , for describing the mid-plane stress resultants  $(\sigma_r \text{ and } \sigma_\theta)$  as

$$\sigma_r = \frac{1}{r} \frac{d\Phi}{dr} \quad \& \quad \sigma_\theta = \frac{d^2\Phi}{dr^2}. \tag{C9} \label{eq:c9}$$

The corresponding in-plane strains  $(\epsilon_r \text{ and } \epsilon_\theta)$  are given as,

$$\epsilon_r = \frac{1}{E}(\sigma_r - v\sigma_\theta)$$
 &  $\epsilon_\theta = \frac{1}{E}(\sigma_\theta - v\sigma_r)$ . (C10)

The nonlinearity associated with the dome inversion and the ensuing bistable behavior is modeled by using nonlinear strain–displacement relationships that allow for large displacements but maintain low strains. This relationship is expressed in the radial co-ordinates as

$$\epsilon_r = \frac{\mathrm{d} u_r}{\mathrm{d} r} + \left[ \frac{1}{2} \left( \frac{\mathrm{d} w}{\mathrm{d} r} \right)^2 - \frac{1}{2} \left( \frac{\mathrm{d} w^0}{\mathrm{d} r} \right)^2 \right] \quad \& \quad \epsilon_\theta = \frac{u_r}{r}. \tag{C11}$$

In order to express the in-plane stresses and strains purely in terms of the generalized co-ordinates, we model the stretching-bending interaction be connecting the change in Gaussian curvature to the in-plane strains and by extension, the Airy's stress function as

$$-E\hat{g} = \frac{d^4\Phi}{dr^4} + \frac{2}{r} \frac{d^3\Phi}{dr^3} - \frac{1}{r^2} \frac{d^2\Phi}{dr^2} + \frac{1}{r^3} \frac{d\Phi}{dr}.$$
 (C12)

Solving this equation, the complete solution for each region consists of the homogeneous solution (expressed in terms of r) and the particular solution, that is expressed as,

$$D_1 + D_2 \text{Log}[r] + \frac{1}{2} D_3 r^2 + D_4 r^2 \left( -\frac{1}{4} + \frac{1}{2} \text{Log}[r] \right). \tag{C13} \label{eq:c13}$$

We note that four additional constants are added in the respective solutions for each region. Taking derivatives to find the mid-plane stress resultants, these constants subsequently appear in the respective expressions in the following form,

$$\sigma_r = D_2 \frac{1}{r^2} + D_3 + D_4 \text{Log}[r] + \dots \quad \& \quad \sigma_\theta = -D_2 \frac{1}{r^2} + D_3 + D_4 (1 + \text{Log}[r]) + \dots$$
 (C14)

This set of six additional constants (three for each region) is solved for by employing the in-plane boundary conditions and the in-plane continuity conditions. To begin with, the stress at the center of the dome (R1) cannot be infinite. Hence,  $(D_2)_{R1} = (D_4)_{R1} = 0$ . Next, using the expressions for  $\epsilon_r$  and  $\epsilon_\theta$ , we obtain two distinct expressions for the in-plane displacement field,  $u_r$  for the flat region, R2. However, for real solutions to the problem, both of the obtained expressions for the displacement fields need to be compatible with each other. Solving for the ensuing compatibility equation,  $[u_r(\epsilon_r)]_{R2} = [u_r(\epsilon_\theta)]_{R2}$ , the constant  $(D_4)_{R2}$  is determined. The remaining three constants  $(D_3)_{R1}$ ,  $(D_2)_{R2}$ , and  $(D_3)_{R2}$  are determined by solving for the in-plane pinned BC at the outer edge,

$$(u_r)_{R2}\big|_{r=b} = 0,$$
 (C15)

and the continuity conditions for the in-plane displacement and the circumferential stress at the shared boundary,

$$(u_r)_{R1}\big|_{r=a} = (u_r)_{R2}\big|_{r=a}$$
 &  $(\sigma_\theta)_{R1}\big|_{r=a} = (\sigma_\theta)_{R2}\big|_{r=a}$ . (C16)

With these simplifications, all of the quantities in the in-plane and out-of-plane problem are unambiguously expressed purely in terms of the generalized co-ordinates,  $c_i$ , and the radial co-ordinate, r. The bending and stretching energy contributions ( $\Pi_B$  and  $\Pi_S$ ) for each of the two regions can be subsequently expressed as,

$$\Pi_{\text{B}} = \frac{1}{2} \int_{\Omega} (\hat{\kappa}_r m_r + \hat{\kappa}_{\theta} m_{\theta}) dA \qquad \& \qquad \Pi_{\text{S}} = \frac{t}{2} \int_{\Omega} (\epsilon_r \sigma_r + \epsilon_{\theta} \sigma_{\theta}) dA. \tag{C17}$$

Adding the bending and stretching energy contributions for both the dome and the flat region  $(\Pi = (\Pi_B)_{R1} + (\Pi_S)_{R1} + (\Pi_B)_{R2} + (\Pi_S)_{R2})$ , local minima in the total potential energy expression are determined by employing the *FindMinimum* function in Mathematica. These local minimum energy points correspond to equilibrium configurations of the unit, i.e., the base state and the inverted state. The stability of each of the equilibrium points is confirmed by evaluating the positive definiteness of the Hessian Matrix  $H_{ij} = \frac{\partial^2 \Pi}{\partial t^2 Dt}$ .

For generality and in order to improve the computational efficiency of the model, we express the unit geometry in terms of three non-dimensional parameters - the shallowness (SH = h/a), slenderness (SL = h/t) and packing factor (PK = 2b/a). Additionally, we non-dimensionalize the field variables for both the regions R1 and R2 in the following manner,

$$\rho = \frac{r}{a}, \quad \omega = \frac{w}{t}, \quad K = \kappa \frac{a^2}{t}, \quad S = \frac{\sigma a^2}{Et^2}, \quad \& \quad M = \frac{ma^2}{Et^4}. \tag{C18}$$

Lastly, the generalized co-ordinates,  $c_i$  are also normalized by the dome base radius a to further improve the computational efficiency of the model. The normalized set of generalized co-ordinates is defined as

$$\hat{c}_i = \frac{c_i}{a}.\tag{C19}$$

The results for the unit topology and for predicting the limit of hierarchical multistability in our metasheets are illustrated in Fig. C.3, and are found to be in good agreement with experimental results.

### Appendix D. Post-buckling mode transition: From mirrorbuckled to elliptical inversion modes

The static bistability of doubly-curved shells or domes has been extensively studied and analyzed in literature [52–56,51,31,57]. The dominant deformation mode involved in dome inversion is the axisymmetric mirror-buckled mode. However, while the second stable state is largely axisymmetric, asymmetric configurations have been found to emerge while the dome is transitioning from one state to the other [30,31]. These asymmetric modes have been largely studied under the context of the dome deformation when subjected to a point load at the apex. Notably, higher order polygonal post-buckling modes have been found during such localized loading cases [30–32]. These higher order polygonal modes feature a strong stretching-bending interaction as compared to the mirror-buckled mode, where the deformation is largely

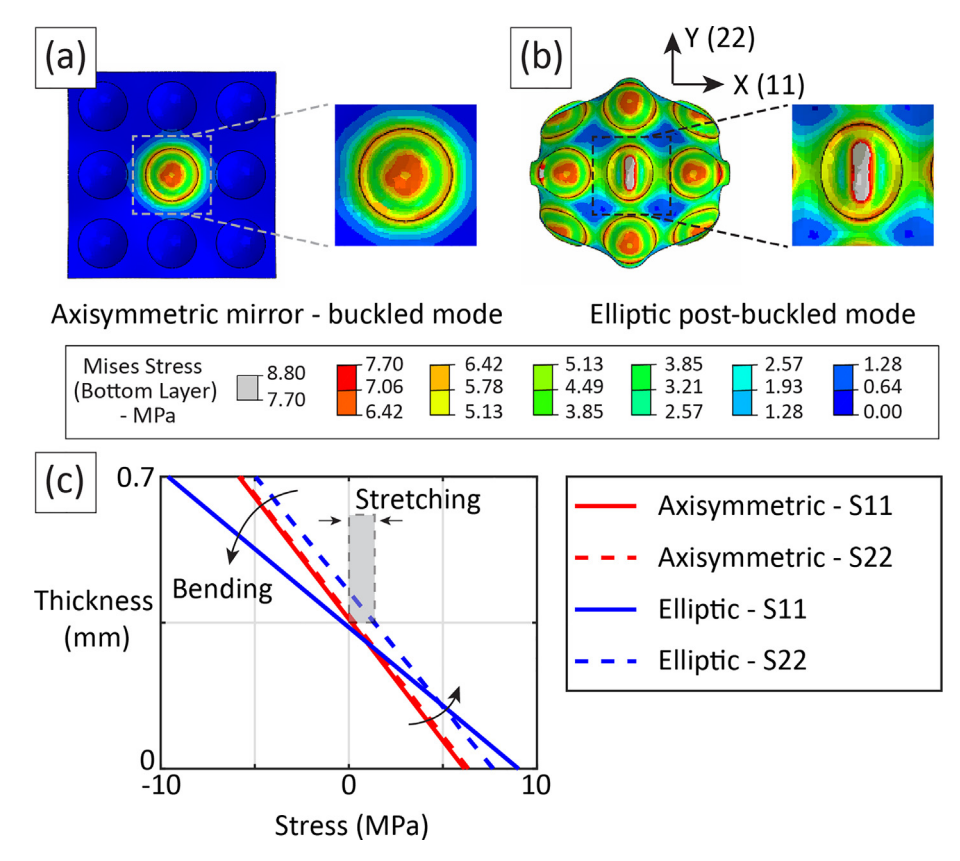


Fig. D.1. (a) The axisymmetric mirror-buckled deformation mode when a single dome is inverted in the metasheet. (b) The elliptic post-buckled deformation mode on the center dome when all domes are inverted and the metasheet assumes a higher order frustrated state. (c) The through-thickness stress fields for the center point on the center dome for the metasheet deformation states in (a) and (b).

bending-dominated [31,32,56]. As illustrated in Figs. 2, 3 in the main text, we find these higher order post-buckling modes in our system as well, although these appear in a qualitatively different context. In our system, such modes emerge due to the asymmetry in the design of the unit planform geometry and are found to originate from the unit boundary. Consequently, they start to localize away from the dome center as the mesoscale packing factor is increased. Importantly, these higher order post-buckled modes play a crucial role in the hierarchical multistable behavior in our metasheets. A single dome inverted in any metasheet features a largely axisymmetric shape and assumes the mirror-buckled configuration (Fig. D.1a). However, we notice that as an increasing number of domes are inverted in the metasheet, interactions start developing between neighboring inverted units. This results in post-buckled shapes that are driven by: (i) the unit geometry; (ii) the state of the neighboring units: and (iii) the sequence in which the interactions are imposed. This feature is distinctly seen on the center dome in the higher-order frustrated state for a  $3 \times 3$  metasheet, as illustrated in Fig. D.1b. The center dome's deformation state departs from the axisymmetric mirror-buckled state and assumes an elliptical post-buckled shape with major axis aligned with the vertical (Y-direction) dimension of the metasheet. Analyzing the through-thickness stress fields in the X- (11) and Ydirections (22) for the center point of the respective units (Fig. D.1c), we find that for the axisymmetric mode, the throughthickness fields are qualitatively similar and are bending dominated. In contrast, for the higher-order frustrated state, the axisymmetry is clearly lost with the stress-fields in the respective directions exhibiting qualitatively different behavior. Furthermore, the stretching-bending interaction for the elliptic post-buckled shape is apparent for the through-thickness field in the Ydirection, in contrast to the mirror-buckled state where this feature is absent and the deformation is bending dominated. This distinct switching behavior between purely bending dominated to a combined stretching-bending deformation state controls the symmetry breaking of the post-buckled mode on the individual domes. These interactions between the stretching and bending behavior within the microstructure of our metasheets are central for the manifestation of macroscale geometric frustration and hierarchical multistable behavior.

# Appendix E. Geometric scalability and material independence of hierarchical multistability

Hierarchical multistability is a geometrically scalable phenomenon and correspondingly, the ground states and higher order frustrated states are also observed in metasheets featuring a higher number of microscale units. This phenomenon is illustrated in Fig. 1f, and also in Fig. E.1 illustrating the base state and four hierarchical multistable states for the  $5 \times 5$  metasheet when all domes are inverted. Furthermore, we note that the manifestation of macroscale geometric frustration, and the ensuing hierarchically multistable behavior of our metasheets are purely geometric features and independent of the material properties as long as the dome inversion-induced stresses are within the failure limits for the corresponding material. We demonstrate this by employing a Nylon metasheet consisting of domes arranged in a  $3 \times 3$  square pattern (Fig. E.2a). Nylon has an elastic modulus of 579 MPa, i.e. is  $22 \times \text{more than TPU } [58]$ . With a glass transition temperature above 50°C, Nylon shows no viscoelastic effect at room temperature. All domes in the Nylon-made metamaterial sheet have uniform dimensions with height h = 4 mm, base radius R = 12 mm, thickness t = 0.4 mm and unit side length SS = 28 mm. Locally, each individual dome features two stable configurations: the asprinted base state and the inverted state. At the global scale, the nylon sheet is again found to exhibit hierarchical multistability with the emergence of the ground states (Fig. E.2a) and the higher-order frustrated states (Fig. E.2c) when all the domes are inverted. This result indicates that geometric frustration and the ensuing hierarchical multistability features are manifested purely due to the geometry of the metasheets and are compatible with different material chemistries. Concretely, material viscoelastic effects observed in many of the soft material systems are not necessary for hierarchical multistability to emerge.

### Appendix F. List of Supplementary Videos

- 1. Inversion of a single dome unit.
- 2. Shifting between the hierarchically multistable states of a  $3 \times 3$  square metasheet by means of external loads.



Fig. E.1. Experimental images of the base state and the hierarchical multistable states when all domes are inverted for the  $5 \times 5$  square metasheet.

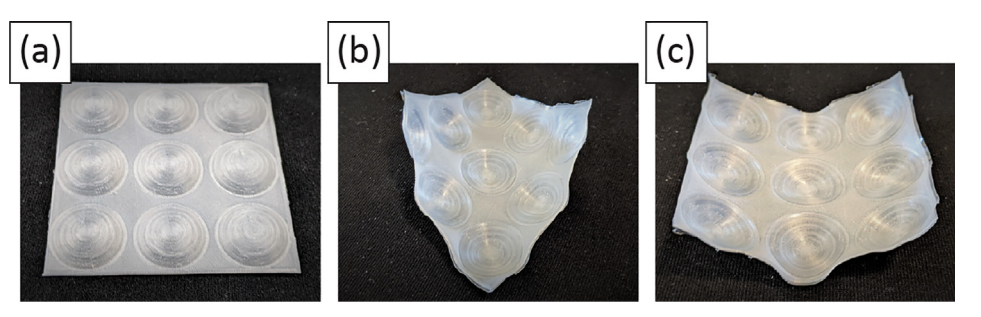


Fig. E.2. Experimental images of the base state and the hierarchical multistable states when all domes are inverted for the 3 × 3 Nylon metasheet.

- 3. The hierarchically multistable states of a hexagonal patterned metasheet
- 4. Diagonal dome inversion sequence leading to a ground state on a 3 × 3 square metasheet.
- 5. Symmetric dome inversion sequence leading to a higher order frustrated state on a  $3 \times 3$  square metasheet.
- 6. Inversion sequence leading to a higher order frustrated state on a  $5 \times 5$  square metasheet.

#### Appendix G. Supplementary material

Supplementary data associated with this article can be found, in the online version, at https://doi.org/10.1016/j.matdes.2022. 110809.

#### References

- [1] R. Moessner, A.P. Ramirez, Geometrical frustration, Phys. Today 59 (2006) 24.
- [2] Y. Han, Y. Shokef, A.M. Alsayed, P. Yunker, T.C. Lubensky, A.G. Yodh, Geometric frustration in buckled colloidal monolayers, Nature 456 (2008) 898.
- [3] G.M. Grason, Perspective: Geometrically frustrated assemblies, J. Chem. Phys. 145 (2016), https://doi.org/10.1063/1.4962629.
- [4] G.H. Wannier, Antiferromagnetism. The triangular Ising net, Phys. Rev. 79 (1950) 357.
- [5] R.M. Houtappel, Order-disorder in hexagonal lattices, Physica 16 (1950) 425.
- [6] A.P. Ramirez, Strongly geometrically frustrated magnets, Annu. Rev. Mater. Sci. 24 (1994) 453.
- [7] R. Siddharthan, B.S. Shastry, A.P. Ramirez, A. Hayashi, R.J. Cava, S. Rosenkranz, Ising pyrochlore magnets: Low-temperature properties, "ice rules, and beyond, Phys. Rev. Lett. 83 (1999) 1854.
- [8] B.C. Dem Hertog, M.J. Gingras, Dipolar interactions and origin of spin ice in ising pyrochlore magnets, Phys. Rev. Lett. 84 (2000) 3430.
- [9] R.F. Wang, C. Nisoli, R.S. Freitas, J. Li, W. McConville, B.J. Cooley, M.S. Lund, N. Samarth, C. Leighton, V.H. Crespi, P. Schiffer, Artificial'spin ice' in a geometrically frustrated lattice of nanoscale ferromagnetic islands, Nature 439 (2006) 303.
- [10] Y. Qi, T. Brintlinger, J. Cumings, Direct observation of the ice rule in an artificial kagome spin ice, Phys. Rev. B Condensed Matter Mater. Phys. 77 (2008) 1.
- [11] J.P. Morgan, A. Stein, S. Langridge, C.H. Marrows, Thermal ground-state ordering and elementary excitations in artificial magnetic square ice, Nat. Phys. 7 (2011) 75.
- [12] S.A. Daunheimer, O. Petrova, O. Tchernyshyov, J. Cumings, Reducing disorder in artificial kagome ice, Phys. Rev. Lett. 107 (2011) 1.
- [13] F. Leoni, Y. Shokef, Attraction Controls the Inversion of Order by Disorder in Buckled Colloidal Monolayers, Phys. Rev. Lett. 118 (2017) 1.
- [14] P. Mellado, A. Concha, L. Mahadevan, Macroscopic magnetic frustration, Phys. Rev. Lett. 109 (2012) 1.
- [15] P. Wang, Y. Zheng, M.C. Fernandes, Y. Sun, K. Xu, S. Sun, S.H. Kang, V. Tournat, K. Bertoldi, Harnessing Geometric Frustration to Form Band Gaps in Acoustic Channe Lattices, Phys. Rev. Lett. 118 (2017) 1.
- [16] C.K. Harnett and C.J. Kimmer, Digital Origami From Geometrically Frustrated Tiles, in Proceedings of the ASME 2013 International Design Engineering Technical Conferences and Computers and Information in Engineering Conference (Portland, Oregon, 2013) pp. 1–9.
- [17] F. Lechenault, B. Thiria, M. Adda-Bedia, Mechanical response of a creased sheet, Phys. Rev. Lett. 112 (2014) 1.
- [18] S. Hoon, S. Shan, A. Košmrlj, W.L. Noorduin, S. Shian, J.C. Weaver, D.R. Clarke, K. Bertoldi, Complex Ordered Patterns in Mechanical Instability Induced Geometrically Frustrated Triangular Cellular Structures, Phys. Rev. Lett. 112 (2014) 098701.
- [19] D.M. Hall, I.R. Bruss, J.R. Barone, G.M. Grason, Morphology selection via geometric frustration in chiral filament bundles, Nat. Mater. 15 (2016) 727.
- [20] M. Lenz, T.A. Witten, Geometrical frustration yields fibre formation in selfassembly, Nat. Phys. 13 (2017) 1100.
- [21] A.P. Ramirez, Geometric frustration: Magic moments, Nature 421 (2003) 483.
- [22] C. Merrigan, C. Nisoli, and Y. Shokef, Topological memory and hysteresis in icelike mechanical metamaterials, arXiv, 1 (2020).
- [23] K.A. Seffen, Mechanical memory metal: a novel material for developing morphing engineering structures, Scripta Mater. 55 (2006) 411.
- [24] J.A. Faber, J.P. Udani, K.S. Riley, A.R. Studart, A.F. Arrieta, Dome-Patterned Metamaterial Sheets, Adv. Sci. (2020) 2001955.

- [25] E.H. Mansfield, Bending, buckling and curling of a heated thin plate, Proc. Roy. Soc. London. Ser. A. Math. Phys. Sci. 268 (1962) 316.
- [26] E.H. Mansfield, Bending, buckling and curling of a heated elliptical plate, Proceedings of the Royal Society of London. Series A. Mathematical and Physical Sciences 288.1414, 396
- [27] K.A. Seffen, Hierarchical multi-stable shapes in mechanical memory metal, Scripta Materialia 414 56, 417 (2007).
- [28] J.P. Udani, A.F. Arrieta, Programmable mechanical metastructures from locally bistable domes, Extreme Mech. Lett. 42 (2021) 101081.
- [29] B.D. Metcalf, Ground state spin orderings of the triangular Ising model with the nearest and next nearest neighbor interaction, Phys. Lett. 46A (1974) 325.
- [30] J.R. Fitch, The buckling and post-buckling behavior of spherical caps under concentrated load, Int. J. Solids Struct. 4 (1968) 421.
- [31] M. Taffetani, X. Jiang, D.P. Holmes, and D. Vella, Static bistability of spherical caps, Proceedings A (2018)
- [32] A. Vaziri, L. Mahadevan, Localized and extended deformations of elastic shells, Proc. Nat. Acad. Sci. 105 (2008) 7913.
- [33] L. Balents, Spin liquids in frustrated magnets, Nature 464 (2010) 199.
- [34] P. Schiffer, A.P. Ramirez, D.A. Huse, A.J. Valentino, Investigation of the Field Induced Antiferromagnetic Phase Transition in the Frustrated Magnet: Gadolinium Gallium Garnet, Phys. Rev. Lett. 73 (1994) 2500.
- [35] O.A. Petrenko, C. Ritter, M. Yethira j, and D.M. Paul, Investigation of the Low-Temperature Spin-Liquid Behavior of the Frustrated Magnet Gadolinium Gallium Garnet, Physical Review Letters 80, 18 (1998).
- [36] I. Mirebeau, I.N. Goncharenko, S.T. Bramwell, P. Cadavez-Peres, S.T. Bramwell, M.J.P. Gingras, J.S. Gardner, Pressure-induced crystallization of a spin liquid, Nature 420 (2002) 54.
- [37] A. Sen, R. Moessner, Topological Spin Glass in Diluted Spin Ice, Phys. Rev. Lett. 114 (2015) 247207.
- [38] E.L. Lawler, D.E. Wood, Branch-And-Bound Methods: A Survey, Oper. Res. 14 (1966) 699.
- [39] S. Kirkpatrick, C.D. Gelatt, M.P. Vecchi, Optimization by Simulated Annealing, Science 220 (2007) 671.
- [40] B. Treml, A. Gillman, P. Buskohl, R. Vaia, Origami mechanologic, Proc. Natl. Acad. Sci. USA 115 (2018) 6916.
- [41] T. Chen, M. Pauly, P.M. Reis, A reprogrammable mechanical metamaterial with stable memory, Nature 589 (2021) 386.
- [42] G. Kofod, M. Paa janen, and S. Bauer, Self-organized minimum-energy structures for dielectric elastomer actuators, Applied Physics A: Materials Science and Processing 85, 141 (2006)
- [43] D. Rus, M.T. Tolley, Design, fabrication and control of soft robots, Nature 521 (2015) 467.
- [44] J.R. Raney, N. Nadkarni, C. Daraio, D.M. Kochmann, J.A. Lewis, K. Bertoldi, Stable propagation of mechanical signals in soft media using stored elastic energy, Proc. Natl. Acad. Sci. USA 113 (2016) 9722.
- [45] H.L. Ferrand, A.R. Studart, A.F. Arrieta, Filtered Mechanosensing Using Snapping Composites with Embedded Mechano- Electrical Transduction, ACS Nano 13 (2019) 4752.
- [46] B.S. Homberg, R.K. Katzschmann, M.R. Dogar, D. Rus, Haptic identification of objects using a modular soft robotic gripper, IEEE Int. Conf. Intell. Robots Syst. (2015) 1698.
- [47] S. Li, H. Bai, R.F. Shepherd, H. Zhao, Bio-inspired Design and Additive Manufacturing of Soft Materials, Machines, Robots, and Haptic Interfaces, Angewandte Chemie - International Edition 58 (2019) 11182.
- [48] K.R. Olympio, F. Gandhi, Flexible Skins for Morphing Aircraft Using Cellular Honeycomb Cores, J. Intell. Mater. Syst. Struct. 21 (2010) 1719.
   [49] F. Runkel, G. Ramstein, G. Molinari, A.F. Arrieta, P. Ermanni, Mechanics of
- [49] F. Runkel, G. Ramstein, G. Molinari, A.F. Arrieta, P. Ermanni, Mechanics of curved-ligament hexachiral metastructures under planar deformations, J. Mech. Phys. Solids 125 (2019) 145.
- [50] Ultimaker, Technical data sheet Ultimaker TPU 95A,, 1 (2018).
- [51] P.M. Sobota, K.A. Seffen, Effects of boundary conditions on bistable behaviour in axisymmetrical shallow shells, Proceedings of The Royal Society A 473 (2017) 20170230.
- [52] E.L. Reiss, H.J. Greenberg, H.B. Keller, Nonlinear Deflections of Shallow Spherical Shells, Journal of the Aeronautical Sciences 24 (1957) 533.
- [53] H.B. Keller, E.L. Reiss, Spherical Cap Snapping, Journal of the Aerospace Sciences 26 (1959) 643.
- [54] G.W. Brodland, H. Cohen, Deflection and snapping of spherical caps, Int. J. Solids Struct. 23 (1987) 1341.
- [55] A. Brinkmeyer, M. Santer, A. Pirrera, P.M. Weaver, Pseudo-bistable self-actuated domes for morphing applications, Int. J. Solids Struct. 49 (2012) 1077.
- [56] K.A. Seffen, S. Vidoli, Eversion of bistable shells under magnetic actuation: a model of nonlinear shapes, Smart Mater. Struct. 25 (2016) 065010.
- [57] L. Stein-Montalvo, P. Costa, M. Pezzulla, D.P. Holmes, Buckling of geometrically confined shells, Soft Matter 15 (2019) 1215.
- [58] Ultimaker, Technical data sheet: Nylon, 1, 2017.